PHYSICAL REVIEW A **66**, 053416 (2002)

Microwave ionization of alkali-metal Rydberg states in a realistic numerical experiment

Andreas Krug and Andreas Buchleitner
Max-Planck-Institut für Physik komplexer Systeme, Nöthnitzer Straße 38, D-01187 Dresden, Germany

(Received 4 July 2002; published 26 November 2002)

We describe an original approach for the accurate description of alkali-metal Rydberg states exposed to intense electromagnetic fields. Our method combines Floquet and *R*-matrix theory, complex dilation of the Hamiltonian, a Sturmian basis set to describe the atomic degrees of freedom (including the continuum), and, last but not least, an efficient parallel implementation of the Lanczos algorithm on some of the most powerful supercomputers currently available. Without adjustable parameters, this *ab initio* approach opens a route to the comprehensive understanding of an abundance of laboratory data on the microwave ionization of one-electron Rydberg states. The versatility of our theoretical/numerical machinery is illustrated in the specific case of microwave driven lithium, faithfully mimicking every single step of the laboratory experiment.

DOI: 10.1103/PhysRevA.66.053416 PACS number(s): 32.80.Rm, 05.45.Mt, 72.15.Rn

I. INTRODUCTION

For more than two decades, periodically driven one-electron Rydberg states of hydrogen [1] and of alkali-metal atoms [2] are amongst the preferred, experimentally accessible objects to study the transition from regular and predictable to highly complex dynamics in simple quantum systems exposed to strong perturbations. Whilst the Keplerian dynamics of a Rydberg electron on its elliptic orbit around the nucleus incarnates the correspondence between the microscopic quantum world and the clocklike precision of planetary motion [3], chaos invades the electron's classical phase space when it is subject to an oscillating force near resonant with the classical Kepler frequency [4–7]. Much like a comet on a chaotic trajectory [8], which finally disappears in the depth of outer space, the Rydberg electron will finally *ionize* in a laboratory experiment on the real, and this is on the quantum-mechanical atom, upon absorption of, say, approximately 10, . . . ,100 photons from the low-frequency driving field in the microwave regime. Remember that, as an immediate corollary of the correspondence principle, a driving field frequency that is resonant with the classical Kepler motion is resonant with the atomic transition $n_0 \rightarrow n_0+1$ between the neighboring Rydberg manifolds labeled by the principal quantum number n_0 (inherited from the classical principal action, via Bohr's quantization). This is the origin of the experimentalist's choice of microwave frequencies when he aims at realizing the chaotic escape of a comet on the atomic scale. However, from a more traditional quantum-mechanical point of view based on our understanding of the photoelectric effect or on common intuition on high-order terms in perturbative expansions, efficient ionization mediated by high-order transition amplitudes from the atomic initial state to the atomic continuum is rather unexpected. Moreover, as realized in the early days of quantum mechanics [9], the highly suggestive quantum-classical correspondence, built on the semiclassical analogy between the hydrogen atom and a planet's orbit around the sun, does not carry over in a simple way to Hamiltonian systems with nonintegrable classical dynamics. It is therefore by no means obvious that efficient (chaotic) ionization of a Rydberg electron can indeed be induced by a microwave field, and yet, by now, this is an experimentally well-established fact [1,10–12]. Put differently, this very experimentalobservation is arguably one of the most dramatic and most tangible fingerprints of chaos in real quantum systems, and hence, of the prevalence of quantum-classical correspondence beyond regular dynamics. Let us also note here that dynamical localization [13–15], a quantum interference effect that decreases the experimentally observed ionization yield as compared to the classical prediction, in a certain parameter regime (which we shall come back to in the sequel of this paper), does *not* obliterate this statement. On the contrary, precisely the classically nonintegrable dynamics provides the indispensable randomization [16] of the quantum-mechanical transition matrix elements, which allows for a globally destructive interference correction to the classical transport coefficient.

However, how to interprete such fingerprints of classical chaos in the quantum dynamics, if no classical Hamiltonian dynamics can be unambiguously identified? Indeed, as implicit in the above argument, ‘‘chaotic’’ ionization and dynamical localization are even observed for one-electron alkali-metal Rydberg states of lithium, sodium, and rubidium, without the availability of a well-defined, classical one-electron Hamiltonian—different phenomenological classical potentials lead to the same quantum spectrum of the unperturbed atom upon quantization [17–19]. Furthermore, all available experimental data [12,20,22] suggest [21] that periodically driven, nonhydrogenic initial states of alkali atoms (i.e., low-angular-momentum states with nonvanishing quantum defects δ_ℓ) exhibit *dramatically enhanced* ionization as compared to atomic hydrogen, whereas hydrogenic initial states also display hydrogenic yields [2]. Hence, there is an abundance of laboratory results that remain to be reconciled with each other, and with the above picture, beyond hand waving arguments that consider alkali-metal Rydberg states as essentially equivalent to Rydberg states of atomic hydrogen. As a matter of fact, for reasons of experimental convenience, almost all of the different experiments [1,2,11,12,20,22–25] performed on the different atomic species were so far performed in slightly different parameter regimes—i.e., under slightly different physical conditions—which is not the optimum demarche to identify the origin of physically different behavior in a ‘‘chaotic’’ setting, i.e., under conditions of a strong sensitivity of the system's response to initial and/or boundary conditions. Therefore, only recently [26–29] some of the different pieces of this puzzle have been put together in a numerical experiment that compares the ionization dynamics of different atomic species under *precisely identical* conditions, for typical laboratory parameters ($n_0 = 28, \ldots, 80$, the driving field frequency being 36 GHz). In the present contribution, we will expand on the details of the theoretical/numerical framework of the emerging picture, and complement some of the results presented in Refs. [27,29].

The paper is organized as follows. Section II presents our theoretical "setup" based on an exact description of the atom in the field, without adjustable parameters, which is notably designed for direct access to the detailed spectral structure underlying the quantum transport problem we are dealing with. Section III accounts for the numerical implementation of our setup in an actual numerical experiment, with some details on numerical convergence and on memory requirements. Section IV presents a numerical experiment on nonhydrogenic Rydberg states of lithium, which faithfully mimics each single step of the laboratory experiment. Besides a direct comparison of lithium and hydrogen ionization dynamics over a broad parameter range, we also discuss the role of the atom-field interaction time as an additional, experimentally controllable [2,12] parameter. Section V concludes the paper.

II. THEORY

The object we have to describe here with a minimum of approximations is a Rydberg atom exposed to a periodic, monochromatic driving field. The Rydberg electron moves in three-dimensional configuration space, subject to the combined potentials of the nucleus and, possibly, of the multielectron core, and is driven and eventually ionized by the external field. Our theoretical description therefore has to account for the following:

(i) the unperturbed one-electron dynamics within a Coulomb-like potential, amended by the multielectron core;

(ii) the spectrum of the atom "dressed" by (i.e., in the presence of) the field, including the atomic continuum;

(iii) the parameter dependence of the ionization process, where the parameter space is spanned by the quantum numbers that define the initial atomic state $|n_0\ \ell_0\ m_0\rangle$ (ℓ_0 and m_0 stand for the angular momentum and its projection on the quantization axis, respectively), and by the amplitude F, the angular frequency ω, and the interaction time t, which characterize the driving field.

To do so, we have to combine various tools as follows.

Let us start with the Hamiltonian of an atom with one active electron, exposed to a linearly polarized microwave field of frequency $\omega = 2\pi/T$ and amplitude F. In dipole approximation, employing the length gauge and neglecting relativistic and QED effects, the Hamiltonian in atomic units reads

$$H(t) = \frac{\mathbf{p}^2}{2} + V_{\text{atom}}(r) + \mathbf{F}\cdot\mathbf{r}\cos\omega t, \quad r>0, \tag{1}$$

where $V_{\text{atom}}(r)$ denotes the atomic potential seen by the valence electron, which we shall specify later. Since Eq. (1) is periodic in time, i.e.,

$$H(t+T) = H(t), \quad \text{with } T = 2\pi/\omega, \tag{2}$$

we can make use of the Floquet theorem [30–32] to access the eigenstates $|\varepsilon_j\rangle$ and eigenvalues ε_j of the atom in the field, which solve the stationary eigenvalue problem

$$\mathcal{H}|\varepsilon_j\rangle = \varepsilon_j|\varepsilon_j\rangle \tag{3}$$

on the extended Hilbert space of square integrable, time-periodic functions $\mathcal{L}^2(\mathbb{R}^3)\otimes\mathcal{L}^2(\mathbb{T}_\omega)$.[1] The latter is the domain of the Floquet Hamiltonian

$$\mathcal{H} = H - i\partial_t, \tag{4}$$

the spectrum of which is invariant under translations by ω. Knowledge of the $|\varepsilon_j\rangle$ and ε_j inside a given Floquet zone (the equivalent of a Brillouin zone in solid-state physics [33]) of width ω is therefore sufficient for a complete description of the dynamics. Introducing the Fourier components of the Floquet eigenstates $|\varepsilon_j\rangle$,

$$|\varepsilon_j\rangle = \sum_{k=-\infty}^{k=+\infty} \exp(-ik\omega t)|\varepsilon_j^k\rangle, \tag{5}$$

we can recast the periodically time-dependent problem (3) into the following coupled set of time-independent equations:

$$\begin{aligned}\left(\frac{\mathbf{p}^2}{2} + V_{\text{atom}}(r)\right)|\varepsilon_j^k\rangle + \frac{\mathbf{F}\cdot\mathbf{r}}{2}(|\varepsilon_j^{k+1}\rangle + |\varepsilon_j^{k-1}\rangle)\\ = (\varepsilon_j + k\omega)|\varepsilon_j^k\rangle, \quad k\in\mathbb{Z},\end{aligned} \tag{6}$$

where the additional quantum number k counts the number of photons exchanged between the atom and the field [32].

Since k is running from $-\infty$ to $+\infty$ in Eq. (6), the dipole term in Eq. (1) couples all bound states of the field-free Hamiltonian to the atomic continuum. Therefore, the spectrum of Eq. (6) no longer consists of a discrete and a continuum part, but rather of resonance states with quasienergies ε_j, and finite lifetimes $1/\Gamma_j$, embedded in the continuum [34]. Precisely the ionization rates Γ_j will finally determine the experimentally measured ionization yield of the atom, for a specific choice of the field parameters. To extract these quantities from Eq. (6), we use the method of complex dilation [34–40], which allows to separate the resonance states from the continuous part of the spectrum. Complexification of the position and momentum operators according to

$$r \rightarrow r\exp(i\theta), \quad p \rightarrow p\exp(-i\theta) \tag{7}$$

---

[1] With $\mathbb{T}_\omega = \mathbb{R}\backslash(2\pi/\omega)$ the unit circle.

transforms the Floquet Hamiltonian in a complex symmetric operator with complex eigenvalues. More precisely, the spectrum of the dilated Hamiltonian has the following properties [34–36,38]:

(a) The spectrum is periodic with period ω, as for the original Hamiltonian.

(b) There are continuous spectra along half lines starting at energies $k\omega$ (i.e., at multiphoton ionization thresholds), rotated away from the positive-energy axis into the lower complex plane, by an angle -2θ.

(c) There are isolated complex eigenvalues $\varepsilon_j = E_j - i\Gamma_j/2$ in the lower half plane, corresponding to the resonance states of $\mathcal{H}$. They are stationary under changes of θ, provided the dilation angle is large enough to uncover their location on the second Riemannian sheet of the resolvent of $\mathcal{H}$. The associated eigenfunctions are square integrable, in contrast to the eigenfunctions of the undilated Hamiltonian, which are outgoing waves [37].

(d) Apart from exceptional values of F and ω, there are no real eigenvalues, since under periodic driving all atomic bound states turn into decaying states.

Once $\mathcal{H}$ has been subjected to the nonunitary transformation [39] induced by Eq. (7), all relevant physical information is therefore directly obtained by a subsequent diagonalization.

While our above discussion is valid for any atomic (or ionic) system with one active electron, at this point we need to specify the atomic potential in Eqs. (1) and (6). Whereas for atomic hydrogen, V_{atom} is given by the attractive Coulomb potential $-1/r$, no uniquely defined one-particle potential is available for multielectron atoms. Therefore, we generalize a variant of R-matrix theory, which was used earlier [41] to describe alkali-metal atoms in static electric and/or magnetic fields, to the case of periodically driven systems. Accordingly, we split configuration space in three regions (see Fig. 1), distinguished by the relative strengths of the external and of the multiparticle atomic fields [42]. In region a, i.e., for $0 < r < r_{\text{core}}$ (where r_{core} determines the extent of the atomic core), the amplitude of the external field can be neglected, and the dynamics is governed by complicated multiparticle effects. Here we cannot write down a one-particle wave function for the valence electron. Outside the atomic core, but not far away from the origin (in region b, $r_{\text{core}} < r < r_0$), the external field is still small compared with the field between atomic core and valence electron. In this region, the radial wave function $F_{\ell,E}(r)$ of the Rydberg electron with angular momentum ℓ and energy E can be specified, with the help of quantum-defect theory [43], as a superposition of regular and irregular Coulomb functions $s_{\ell,E}$ and $c_{\ell,E}$,

$$F_{\ell,E}(r) = \cos(\pi\delta_\ell) s_{\ell,E}(r) + \sin(\pi\delta_\ell) c_{\ell,E}(r), \tag{8}$$

where the δ_ℓ denote the angular-momentum-dependent quantum defects that specify the different alkali atoms. Finally, in region c (i.e., for $r \geqslant r_0$), the potential V_{atom} can be described as a Coulomb potential $-1/r$. However, the eigenfunction in region c has to be matched smoothly to the wave function (8) in region b. This determines the phase shift of the alkali-metal Rydberg electron's wave function as compared to the hydrogenic one, due to the scattering of the valence electron off the multiparticle core.

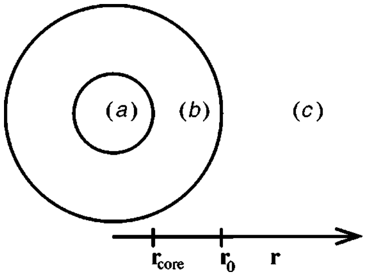

FIG. 1. Division of configuration space for our implementation of the R-matrix method [41,42]. In the inner region a, $r < r_{\text{core}}$, complicated multielectron interactions dominate the dynamics—the multiparticle wave function is unknown. In region b, $r_{\text{core}} < r < r_0$, the force of the driving field on the Rydberg electron is negligible as compared to the influence of the core potential. The Rydberg electron's wave function can be represented as a linear combination (8) of regular and irregular Coulomb functions. In region c, $r > r_0$, the Rydberg electron moves under the combined influence of the driving field and of an effectively hydrogenic Coulomb potential, due to the screening of the nuclear charge by the multielectron core. To obtain the quasienergies ϵ_j and ionization rates Γ_j of the atom in the field, the Floquet eigenvalue problem (6) is solved in the outer region c, with the appropriate boundary condition (10) at the matching radius r_0.

To solve Eq. (6) for alkali-metal Rydberg states, we thus have to substitute $V_{\text{atom}}(r) = -1/r$, in the reduced range $r > r_0 > 0$. However, the operator d^2/dr^2 is no more Hermitian on the interval (r_0, ∞). (Note that the loss of Hermiticity has nothing to do with the complex dilation (7) of position and momentum operators. It simply illustrates that Hermiticity of an operator crucially depends on its domain [44].) To enforce Hermiticity of the second derivative for $r \in (r_0, \infty)$, we have to add a surface term

$$-\delta(r - r_0)\left(\frac{\partial}{\partial r} + C_{\ell,\varepsilon_j}\right) \tag{9}$$

to the Hamiltonian. In the constant term C_{ℓ,ε_j}, the matching condition between regions c and b, and thus the nonhydrogenic phase shift of the alkali-metal wave function for large r is incorporated. We define C_{ℓ,ε_j} as the logarithmic derivative of the wave function $F_{\ell,E}(r) = F_{\ell,\varepsilon_j,k}(r)$, evaluated at energy $\varepsilon_j + k\omega$ (which is an eigenvalue of the Floquet problem) and position r_0:

$$C_{\ell,\varepsilon_j,k} = \frac{1}{F_{\ell,\varepsilon_j,k}(r)} \frac{\partial}{\partial r} F_{\ell,\varepsilon_j,k}(r). \tag{10}$$

Since ε_j is not known beforehand, in principle, an iterative procedure is required to solve Eq. (6) under the constraint (10). Such a procedure, however, guarantees only the convergence of one single eigenvalue ε_j (with the associated eigenvector) which coincides with the energy at which the surface term is evaluated. To obtain more than just one converged eigenvalue per diagonalization we expand the surface term [41], which is a smooth function of energy, in a power series:

$$C_{\ell,\varepsilon_j,k}=C^{(0)}_{\ell,\varepsilon_j,k}+(\varepsilon+k\omega)C^{(1)}_{\ell,\varepsilon_j,k}+\cdots. \tag{11}$$

Instead of the exact term $C_{\ell,\varepsilon_j,k}$, we employ only the constant and the linear terms, $C^{(0)}_{\ell,\varepsilon_j,k}$ and $C^{(1)}_{\ell,\varepsilon_j,k}$, respectively. These are found by computing the Coulomb functions $s_{\ell,\varepsilon_j+k\omega}(r)$ and $c_{\ell,\varepsilon_j+k\omega}(r)$ over a suitable energy grid, and fitting the logarithmic derivative to a linear function. This approach finally allows us to obtain some hundred—instead of one—converged eigenvalues, with one single diagonalization [28] of the eigenvalue problem (6).

The complex dilated Floquet Hamiltonian amended by the core induced surface term is now represented in a suitable basis set. An appropriate choice are the real Sturmian basis functions [45,46]. In spherical coordinates, they are given by the expression

$$\langle r,\theta,\phi|S^{(\alpha)}_{n,\ell,m}\rangle=\mathcal{D}(n,\ell)\exp\left(\frac{-r}{\alpha}\right)\left(\frac{2r}{\alpha}\right)^{\ell}\times L^{(2\ell+1)}_{n-\ell-1}\left(\frac{2r}{\alpha}\right)Y_{\ell,m}(\vartheta,\phi), \tag{12}$$

$$\text{with}\quad \mathcal{D}(n,\ell)=\sqrt{(n-\ell-1)!/(n+\ell)!},\quad |m|\leq\ell<n,$$

where the $Y_{\ell,m}(\vartheta,\phi)$ denote the usual spherical harmonics [47], and $L^{(2\ell+1)}_{n-\ell-1}(r)$ denote the associated Laguerre polynomials [47]. The ideal suitability of the Sturmians for Coulomb (-like) problems consists in the fact that they perfectly match the internal symmetry of the Coulomb potential. Furthermore, they form a discrete basis set that spans the entire Hilbert space, including both the discrete and the continuum part of the spectrum. This is paid by the minor disadvantage that they are orthonormal with respect to a scalar product involving a factor $1/r$, instead of the usual scalar product on $\mathcal{L}_2(\mathbb{R}^3)$. Hence, our eigenvalue problem (6) transforms into a generalized eigenvalue problem of the form

$$(\mathcal{A}-\varepsilon_j\mathcal{B})|\varepsilon_j\rangle=0, \tag{13}$$

where both $\mathcal{A}$ and $\mathcal{B}$ are nondiagonal. However, the integrals defined by the matrix representation of Eq. (13) now become simple expressions, slightly complicated for alkali-metal atoms, but always with strong selection rules. Indeed, for linear polarization of the driving field along the $\hat{z}$ axis, what we shall assume in the following, and after integration of Eq. (13) over the solid angle, we have $\Delta m=0$, due to the rotational symmetry of the problem with respect to the polarization axis,

$$\Delta\ell=0,\quad \Delta k=0, \tag{14}$$

for the atomic part, and

$$\Delta\ell=\pm1,\quad \Delta k=\pm1, \tag{15}$$

for the atom-field coupling term in Eq. (6). These selection rules express that the external (dipole) field couples only the neighboring angular momenta. Hence, changing the angular momentum by one quantum requires the absorption or emission of a photon (which can carry one quantum), and the eigenvalue problem (13) consequently factorizes into two subspaces labeled by the eigenvalues ±1 of the generalized parity,

$$\Pi=(-1)^{\ell+k}, \tag{16}$$

which is conserved by the external field. To obtain all relevant information on the ionization process, the Floquet Hamiltonian has to be diagonalized on both subspaces, which, however, each can be explored with half the total memory requirement.

The flexibility of Sturmian functions is yet enhanced by the real scaling parameter α in Eq. (12), which determines the spatial resolution of the basis. Comparison of Eq. (12) to the analytical form of hydrogen wave functions shows that (apart from normalization constants) the nth bound hydrogen wave function can be identified with the nth Sturmian function, provided that $r_{\mathrm{hydro}}=r_{\mathrm{sturm}}n/\alpha$. Thus, a suitable choice of α enables us to define the spatial region where the basis is optimally adapted to represent the electronic wave function, even for a basis size that is not too large.

In a numerical simulation we obviously have to introduce a cutoff n_{sup} of the Sturmian basis, due to the finite memory of any computer (see also Sec. III). This implies a shift of the continuum threshold towards a value $n^{\mathrm{eff}}_{\mathrm{max}}<\infty$. Since the expectation value of the position operator $\langle r_{\mathrm{hydro}}\rangle$ scales as n^2, the above scaling argument for Sturmians yields $\langle r_{\mathrm{sturm}}\rangle\sim n\alpha$. Hence, the expectation value $\langle r_{\mathrm{sturm}}\rangle$ of the n_{sup}th Sturmian function scales as $n_{\mathrm{sup}}\alpha$, and the effective continuum thresholds $n^{\mathrm{eff}}_{\mathrm{max}}$ and $E^{\mathrm{eff}}_{\mathrm{cont}}$ are given by, respectively,

$$n^{\mathrm{eff}}_{\mathrm{max}}=\sqrt{n_{\mathrm{sup}}\alpha},\quad E^{\mathrm{eff}}_{\mathrm{cont}}=-\frac{1}{2n_{\mathrm{sup}}\alpha}. \tag{17}$$

Note also that in laboratory experiments an effective cutoff quantum number $n^{\mathrm{eff}}_{\mathrm{max}}$ is introduced, i.e., highly excited bound states with $n>n^{\mathrm{eff}}_{\mathrm{max}}$ cannot be distinguished from continuum states. There, the existence of an effective continuum threshold is caused by unavoidable stray electric fields created by contact potentials [10,12] (which, of course, is nothing but an experimental limit to the spectral resolution).

Now all is set to diagonalize the generalized eigenvalue problem (13), in order to obtain the quasienergies ε_j, the decay rates Γ_j, and the associated eigenstates $|\varepsilon_j\rangle$ of the microwave driven atom. These constitute the raw data of our numerical experiment, as illustrated in Fig. 2. The experimental quantity of interest, the ionization probability (averaged over the initial phase of the driving field) at time t of an atom initially prepared in the state $|n_0,\ell_0,m_0\rangle$, is easily deduced through [48]

$$P_{\mathrm{ion}}(t)=1-\sum_{\varepsilon_j}w_j\exp(-\Gamma_j t), \tag{18}$$

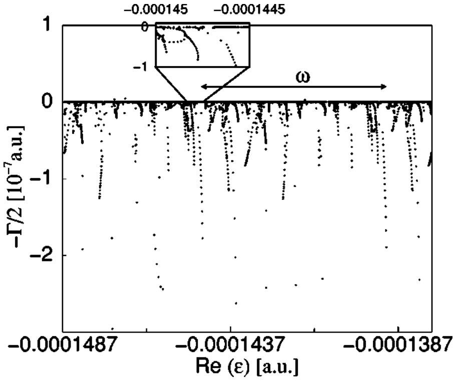

FIG. 2. Complex eigenvalues $\epsilon_j - i\Gamma_j/2$ of the complex dilated Hamiltonian of microwave driven lithium atoms, exposed to a field amplitude $F = 2.3\times 10^{-9}$ a.u. and frequency $\omega/2\pi = 36$ GHz. The plot shows the spectrum in two adjacent Floquet zones, for generalized parity $\Pi = +1$; see Eq. (16). According to the mathematical theory of complex dilation [35,36,38], the continua are rotated in the lower complex plane ("second Riemann sheet"), ideally by an angle -2θ. This is approximately true only very close to the real energy axis, as displayed in the inset [the branching point defined by Eq. (17) is located roughly in the middle of the inset, which extends over an energy range of about $\omega/10$]. The ionization rates Γ_j of the relevant resonances, which contribute to the ionization probability of the desired initial states through nonvanishing weights w_j in Eq. (18), are of the order $\Gamma_j \simeq 10^{-9}$–10^{-13} a.u. They appear as black dots in the immediate vicinity of the (real) energy axis in the plot. Few spurious eigenvalues with positive imaginary parts are also observed, which have to be rejected as physically unacceptable solutions. Since they exhibit vanishing weights w_j, this does not affect the resulting ionization yield.

with w_j the (phase averaged) overlap of the atomic initial state with the atom-field eigenstate $|\varepsilon_j\rangle$ [48]. The sum is understood to run over all eigenstates in one Floquet zone, in both parity subspaces $\Pi = \pm 1$. Since w_j and Γ_j are obtained for a fixed value of the driving field amplitude F, the finite switching time (when the amplitude is ramped from 0 to F, or from F to 0) of the field in any experiment is neglected. Whilst recent experiments on lithium atoms [2], which used a switching time of approximately three field cycles (compared to a total atom-field interaction time of $t > 100$ field cycles), almost realize this ideal situation of a rectangular pulse, earlier experiments [10] switched on a considerably longer time scale (turn on and turn off of $\simeq 50$ field cycles each, flat top of $\simeq 300$ field cycles). However, it is known [49–52] that the pulse envelope has no decisive effect on the experimentally observed onset of ionization, for the typical field strengths and interaction times of microwave ionization experiments, except for specific values of n_0.

Finally, let us note that, unlike methods that propagate an initial wave packet in time (and which, on the other hand, are well suited to track pulse-induced effects), our Floquet approach provides the *complete* spectral information on the driven atom. Since the spectral ingredients of Eq. (18) do neither depend on t nor on the atomic initial state, we can easily determine $P_{\mathrm{ion}}(t)$ for different values of n_0, ℓ_0, and t (m_0 is invariant, due to the rotational symmetry around the field polarization axis), with one single diagonalization. We shall take advantage of this feature in Sec. IV.

III. NUMERICAL IMPLEMENTATION

We have now collected all the tools for an accurate description of the atomic excitation and decay process under periodic driving, without any adjustable parameters. Still, we have to adapt this machinery to the specific physical situation under study, defined by

(1) the quantum defects δ_ℓ of the atomic species,
(2) the atomic initial state $|n_0\ \ell_0\ m_0\rangle$, and
(3) amplitude F and the frequency ω of the driving field.

While the δ_ℓ—obtained from highly accurate spectroscopic experimental data [53]—determine the number of angular-momentum channels with nontrivial matching conditions (10) and (11), the (invariant) value m_0 of the angular-momentum projection sets the minimum value of ℓ, which can be reached during the atomic excitation process, see Eq. (12). In view of the limited memory of any computer, we also seek to impose an upper limit $\ell_{\max}$ on the angular-momentum component of our basis set, without loss of convergence. As a rule-of-thumb, we found $\ell_{\max} \simeq \ell_0 + k_{\max}$ to suffice, where $k_{\max}$ is the upper bound that we impose in the Fourier expansion (5) of the Floquet eigenstates, i.e., in physical terms, the maximum number of photons absorbed by the atom from the field. Obviously, in order to induce efficient population transfer across the effective ionization threshold $E_{\mathrm{cont}}^{\mathrm{eff}}$, Eq. (17), we need $k_{\max} > k_{\mathrm{cont}} = (E_{\mathrm{cont}}^{\mathrm{eff}} - E_0)/\omega$, with $E_0 = -1/2(n_0 - \delta_\ell)^2$ being the energy of the unperturbed atomic initial state. Hence, the order of the relevant multiphoton process increases with decreasing n_0 or ω, and so do $k_{\max}$ and $\ell_{\max}$. In our present treatment, using the length gauge [see Eq. (1)] to allow for a transparent partition of configuration space as illustrated in Fig. 1, we achieved numerical convergence for $k_{\max} \simeq 1.5 k_{\mathrm{cont}}, \ldots, 2 k_{\mathrm{cont}}$, which is a considerably larger photon basis size than reported in Ref. [48]. In these hydrogen calculations, however, no matching condition had to be fulfilled and the velocity gauge—which is known to lead to considerably faster numerical convergence than the length gauge [54,55]—was used. With the above values of $k_{\max}$, $\ell_{\max}$ typically reaches values between $n_{\max}^{\mathrm{eff}}$ and $n_{\mathrm{sup}} - 1$, with the strongest reduction of memory demand for the largest driving field frequencies considered hereafter.

Whereas the maximum number of photons absorbed from the field, $k_{\max}$, clearly may not be smaller than k_{cont}, we can impose a tighter bound on the maximum number of photons emitted into the field, $k_{\min}$. For the typical parameter values considered in the following section, $k_{\min} \simeq -10$ turned out to be a good choice. This dramatic asymmetry in the truncation of the photon component of our basis ($k_{\max}$ can reach values larger than 100!) is a consequence of the anharmonicity of the Rydberg spectrum, which leads to rapidly decreasing transition amplitudes from $|n_0\ \ell_0\ m_0\rangle$ towards lower-lying states [28].

As the last component of our basis set, we have to truncate the principal quantum number n, with an upper limit n_{sup} already introduced in the preceding section. Motivated by the analogy between the finite spectral resolution in the laboratory and in the numerical experiment [see the discussion of Eq. (17) in Sec. II above], we chose n_{sup} and the Sturmian scaling parameter α in such a way that these mimic an effective continuum threshold at $n_{\mathrm{max}}^{\mathrm{eff}} \simeq 104$ (specifically, we set $\alpha = 70$ and $n_{\mathrm{sup}} = 155$), comparable to state of the art experiments with $n_{\mathrm{max}}^{\mathrm{eff}} \simeq 90$ [10], $\simeq 135$ [12], and $\simeq 280$ [2].

Finally, we still have to fix the matching radius r_0 and the dilation angle θ. For our subsequent calculations on lithium with $n_0 = 28, \ldots, 80$, $r_0 = 10, \ldots, 18$ (similar to the radius employed in Ref. [41]) and $\theta = 0.02, \ldots, 0.06$ led to optimal convergence. Note that large values of n_0 favor the numerical stability under changes of r_0, since the larger n_0, the smaller the electronic density close to the matching region [28].

With these premises, we arrive at basis sizes n_{basis} and bandwidths n_{band} of the eigenvalue problem (13) ranging from $n_{\mathrm{basis}} = 279\,072$, $n_{\mathrm{band}} = 4862$ (for atomic initial states in the vicinity of $n_0 = 70$) to $n_{\mathrm{basis}} = 1\,010\,016$, $n_{\mathrm{band}} = 6306$ (for $n_0 \simeq 30$), in our subsequent calculations on lithium. The corresponding quantum defects are $\delta_{\ell=0} = 0.399\,468$, $\delta_{\ell=1} = 0.047\,263$, $\delta_{\ell=2} = 0.002\,129$, and $\delta_{\ell=3} = -7.7 \times 10^{-5}$ [53]. To compute the ionization probability (18) of a specific atomic initial state, not all eigenvalues of these huge matrices are needed, but only those approximately 4000 resonances that have a nonvanishing overlap w_j with the initial state. Since this is a small number compared to n_{basis}, the Lanczos algorithm [48,56,57] is ideally suited to extract the required spectral information from such large matrices. In order to handle their enormous size (approximately 20–97 Gbytes of memory are needed to store the complex symmetric matrices), we use an efficient parallel implementation of the algorithm [58], and work on some of the largest supercomputers (i.e., on the HITACHI SR8000-F1 of the LRZ Munich and the CRAY T3E of the Rechenzentrum Garching) accessible in the academic realm [28,29].

IV. NUMERICAL EXPERIMENTS

Let us now come to the results of our numerical experiment. At first we study typical ionization yields of microwave driven lithium atoms, which exhibit similar qualitative features as observed for microwave driven atomic hydrogen. Here we focus on the dependence of the ionization probability on the laboratory field amplitude, for fixed frequency and variable initial atomic states. From that we will extract the driving field amplitude $F_{10\%}$ which defines the ionization threshold, for different principal quantum numbers, and finally address the apparent differences in the ionization process of alkali-metal and hydrogen atoms.

For the sake of comparison, we choose exactly the laboratory parameters of the experiment reported in Ref. [10], where the microwave ionization of atomic hydrogen was studied. More precisely, we employ a linearly polarized microwave field with fixed frequency $\omega/2\pi = 36$ GHz, and principal quantum numbers $n_0 = 28, \ldots, 80$ of the atomic initial state. Since we are interested in nonhydrogenic effects induced by the atomic core [27–29], we prepare the atoms in low-angular-momentum states $\ell_0 = 0$ with the largest quantum defect $\delta_{\ell_0} = 0.399\,468$ [53]. Note that this is in contrast to the hydrogen experiment [10], where only the principal quantum number n_0 of the initial state was well defined, and ℓ_0 was smoothly distributed over the energy shell. However, since the driving field efficiently mixes different ℓ states [59,60], this does not affect our expectation for the global dependence of the ionization yield on n_0 [52,60].

Let us first come back to Fig. 2, which shows the numerical raw data in the complex plain, obtained from one single diagonalization, for $F = 2.3 \times 10^{-9}$ a.u.$\simeq 11.83$ V/cm and $\omega/2\pi = 8.71 \times 10^{-7}$ a.u.$= 36$ GHz. By virtue of Eq. (18), the imaginary parts $-i\Gamma_j/2$ of the different resonance states, together with the overlaps w_j of the associated eigenstates with the atomic initial state, allow to extract the ionization probability $P_{\mathrm{ion}}(t;F,\omega)$, after summation over all resonances of Fig. 2. It should be noted as a side remark that the present physical situation obviously cannot be described by any sort of single-pole approximation widely used for the description of the ionization of ground-state atoms by optical fields [61]. This is just a consequence of the broad distribution of the w_j and Γ_j (over several orders of magnitude) [12,23,28,51,52,62,63], which is a direct spectral signature of “quantum chaos.” Such broad distributions generically lead to algebraic rather than exponential temporal decay of the survival probability $1 - P_{\mathrm{ion}}$, a resurgent matter of interest in the context of classically mixed regular-chaotic transport [64–68] in mesoscopic devices [69,70].

Furthermore, note that there are few spurious solutions with *positive* imaginary parts in Fig. 2, which have to be rejected as unphysical. Consistently, however, these states always have vanishing overlap with the atomic initial state, and discarding them does not imply a loss of the norm of the initial state represented in the Floquet basis. Zooming into the spectrum in the vicinity of an effective continuum threshold, Eq. (17), the inset of Fig. 2 additionally shows that the numerically obtained spectrum of the complex dilated Hamiltonian does not display a straight-line continuum swept by 2θ into the complex plane, as expected from the mathematical theory [34]. Rather several continua appear to emanate from the branching point, as a consequence of the lifted angular-momentum degeneracy of the continuum states in a truncated basis, interacting with close-by resonances [48,52,71,72].

Figure 2 provides the elementary building block of the numerical experiment, which is reproduced for several values of F, in order to extract the ionization yield as a function of the driving field amplitude. Figure 3 shows the result for five atomic initial states $|n_0, \ell_0 = m_0 = 0\rangle$, with $n_0 = 61,63,65,67,69$, in close qualitative agreement with laboratory ionization yields, and with the characteristic threshold behavior. Below a certain threshold amplitude, the Coulomb field largely dominates the external drive, and the dynamics is governed by the spherical symmetry of the bare atom. This is the perturbative regime where the field does not induce appreciable ionization. Above threshold, the external field

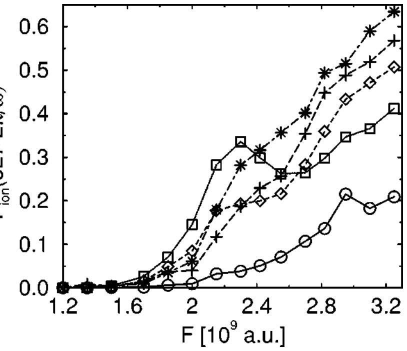

FIG. 3. Ionization probability vs field amplitude F of five different initial states $|n_0,\ell_0=m_0=0\rangle$ of lithium, for $n_0=61$ (circles), 63 (squares), 65 (diamonds), 67 (crosses), and 69 (stars). Atom-field interaction time and driving field frequency are fixed at $t=327\times 2\pi/\omega$ and $\omega/2\pi=36$ GHz, respectively, precisely as in the hydrogen experiment reported in Ref. [10]. On top of the global threshold behavior of all ionization signals there are local structures, most prominent in the local maximum of the $n_0=63$ signal, at $F\simeq 2.3\times 10^{-9}$ a.u. Such local extrema can be attributed to the avoided crossings in the Floquet spectrum, with a corresponding enhancement of the ionization rates, caused by multiphoton resonances that facilitate the electronic transport to the continuum.

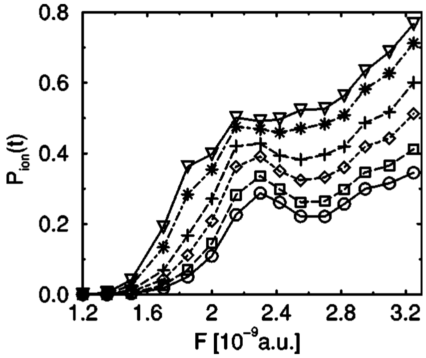

FIG. 4. Ionization probability of the initial state $|n_0=63,\ell_0=m_0=0\rangle$ as a function of the driving field amplitude F, for six different interaction times $t=227\times 2\pi/\omega$ (circles), $327\times 2\pi/\omega$ (squares), $560\times 2\pi/\omega$ (diamonds), $925\times 2\pi/\omega$ (crosses), $2023\times 2\pi/\omega$ (stars), and $3286\times 2\pi/\omega$ (triangles). The frequency is the same as in Fig. 3. Since the time dependence of the ionization probability differs for different values of F [different values of F lead to different distributions of the weights w_j and rates Γ_j, which enter Eq. (18)], the local structure in F changes with increasing interaction time, as evident from the flattening out of the local minimum at $F\simeq 2.3\times 10^{-9}$ a.u., as t is increased from its minimum to its maximum value. The 10% ionization threshold, however, is only weakly affected by changes of the interaction time.

(which has cylindrical symmetry) dominates over the Coulomb attraction, and induces a strong coupling of a large number of atomic bound (and continuum) states, leading to enhanced ionization. This manifests in a steep increase of P_{ion}, and justifies the (traditional) definition of the ionization threshold by that amplitude ($F_{10\%}$) which causes 10% of the atoms to ionize [21]. Besides the threshold structure exhibited by the five curves in Fig. 3, we also observe, in some cases, a local maximum on top of the global trend, most dramatically for $n_0=63$, at $F\simeq 2.3\times 10^{-9}$ a.u.$\simeq$0.42 V/cm. Such a local enhancement of the ionization probability can be attributed to an anticrossing of two Floquet states in the quasienergy spectrum, under changes of the field amplitude [28,51]. Near degeneracies between two atom-field eigenstates at a given field amplitude reflect multiphoton resonances between atomic bound states. These enhance the coupling to the continuum, and thus also the ionization rates Γ_j of the atom-field eigenstates that are involved in the anticrossing. In the present case, the projections w_j of these near-degenerate Floquet states on the atomic initial state $|n_0=63,\ell_0=m_0=0\rangle$ are larger than their projection on those initial states with $n_0=61,65,67,69$, and hence the $n_0=63$ state exhibits a larger ionization probability than the other four states at $F=2.3\times 10^{-9}$ a.u. [see Eq. (18)]. Increasing the field amplitude further, the anticrossing is passed, and the ionization probability of the $n_0=63$ state decreases again.

From the definition (18) of the ionization probability of a given initial state as a weighted sum over the exponentials $\exp(-\Gamma_j t)$ of the ionization rates Γ_j of all atom-field eigenstates, it is clear that P_{ion} depends on the atom-field interaction time [48,51,52,73], in qualitative agreement with laboratory experiments on rubidium [12,23], and, more recently, lithium [2]. In Fig. 4, we plot P_{ion} as a function of F, for the initial state $|n_0=63,m=\ell=0\rangle$, and for several interaction times $t=(227,\dots,3286)\times 2\pi/\omega$. Although neither the global trend of P_{ion} vs F nor the threshold field $F_{10\%}$ depend very sensitively on t, we observe a change in the local structure of the ionization yield. The rather pronounced maximum in the vicinity of $F=2.3\times 10^{-9}$ a.u., for $t=227\times 2\pi/\omega$, flattens out for longer interaction times, until the ionization yield is almost constant in the interval $F=(2.2\times 10^{-9})$–(2.4×10^{-9}) a.u. for $t\simeq 2023\times 2\pi/\omega$. While, at $F=2.3\times 10^{-9}$a.u., the ionization probability is dominated by the ionization rates of the near-degenerate Floquet states (which also cause the maximum of the $n_0=63$ yield in Fig. 3, see our discussion above) on short time scales, these states already decayed for long interaction times. The remaining part of the electronic population is spread over more stable atom-field eigenstates. Hence, as t increases, the atomic decay at $F=2.3\times 10^{-9}$ a.u. slows down as compared to larger field amplitudes, which explains the observed behavior. Let us mention here that a similar observation was recently reported on laboratory experiments on the ionization of hydrogenic initial states of lithium [2]. There [see Fig. 3(a) of Ref. [2]] the ionization probability is essentially flat below threshold for short interaction times, while a shoulderlike structure emerges for longer times t, leading additionally to an observable effect in the experimental ionization threshold (Fig. 4 of Ref. [2]).

Having understood the essential features of the ionization yield of a given atomic initial state, we can now address the dependence of the ionization threshold $F_{10\%}$ on the initial state's principal quantum number. Figure 5(a) compares our numerical lithium thresholds to the results of laboratory experiments on hydrogen [10] and lithium [22], respectively. Whereas the hydrogen experiment was performed under the same conditions as our numerical experiment (see above),

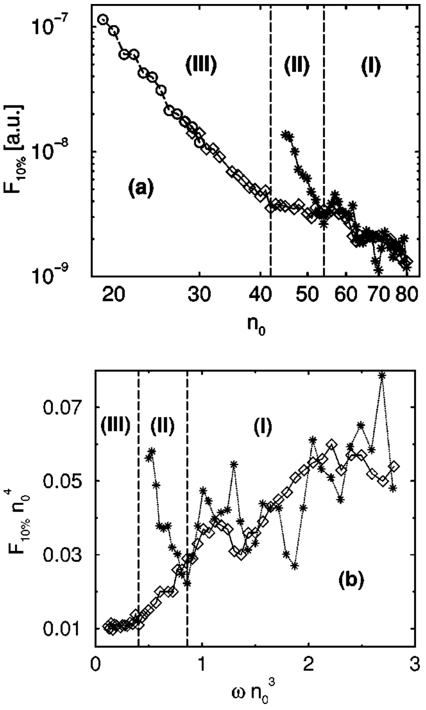

FIG. 5. (a) Numerical ionization threshold $F_{10\%}$ of lithium Rydberg states $|n_0,\ell_0=m_0=0\rangle$ (diamonds), as a function of the principal quantum number n_0, on a double-logarithmic scale. The numerical data are compared to laboratory thresholds [10] of atomic hydrogen (stars) and of lithium (circles) [22]. The numerical and the hydrogen experiment were performed at precisely the same laboratory parameters (frequency $\omega/2\pi=36$ GHz, interaction time $t=327\times 2\pi/\omega$, principal quantum numbers $n_0=28,\ldots,80$), while the lithium results from the laboratory were obtained at lower frequencies ($\omega/2\pi=15$ GHz) and longer interaction times ($t=15000\times 2\pi/\omega$). Alkali-metal and hydrogen thresholds differ qualitatively and quantitatively in regimes (III) and (II), while the numerical alkali-metal thresholds mimic the hydrogenic ones for high principal quantum numbers [regime (I)], and match the alkali-metal thresholds from the laboratory in the low-n_0 regime. (b) Hydrogen and numerical lithium data as in (a), now in scaled variables, $F_{0,10\%}=F_{10\%}n_0^4$ and $\omega_0=\omega n_0^3$ (inherited from the scale invariance of the classical, periodically driven two-body Kepler problem). Since both data sets were obtained for the same values of ω, t, and n_0, a comparison in scaled units does not imply any additional hypothesis on the scaling laws for nonhydrogenic alkali-metal Rydberg states. Clearly, lithium exhibits dynamical localization in regimes (I) and (II), and unexpectedly, the same threshold as hydrogen in the high-frequency domain (I). All laboratory data on nonhydrogenic Rydberg states [2,12,20,23] have so far been produced in regimes (II) and (III), and this explains the experimentally observed enhanced ionization as compared to atomic hydrogen.

the laboratory lithium data have been obtained with a lower driving field frequency $\omega/2\pi=15$ GHz and at longer atom-field interaction times $t=15\,000\times 2\pi/\omega$.

Inspection of Fig. 5 leads to the following observations:

(1) For low principal quantum numbers $n_0\leqslant 42$ [regime (III)], the numerical thresholds show approximately the same algebraic dependence on n_0 as the experimental lithium data.

(2) All three curves exhibit algebraic decay $F_{10\%}\sim n_0^{-\gamma}$, with a clear change of the decay exponent of the (numerical) lithium curve at $n_0=42$ [thus defining the transition from regime (III) to (II)].

(3) For $n_0\gtrsim 54$ [regime (I)], the $m_0=\ell_0=0$ lithium thresholds agree well with the hydrogen results.

As pointed out in Refs. [27–29], the distinct behavior of the (alkali-metal) ionization dynamics in the three regimes, and the differences between the alkali-metal and the hydrogen thresholds, can be explained by the level structure of the different atomic species. In regime (I), the external frequency ω exceeds or equals the splitting between the unperturbed hydrogen manifolds n_0 and n_0+1. Here, the external driving field easily induces a near-resonant one-photon coupling of adjacent hydrogenic (emerging from angular-momentum states with vanishing quantum defects) and nonhydrogenic (emerging from angular-momentum states with nonvanishing quantum defects) energy levels in the alkali-metal atom, much the same as a coupling of adjacent levels in atomic hydrogen.

For lower quantum numbers [in regime (II)], the splitting between unperturbed hydrogenic energy levels exceeds the external driving frequency. Thus, the external field cannot induce efficient mixing of adjacent hydrogen levels any more, and consequently, the experimental hydrogen data change their slope at $n_0\simeq 54$ in Fig. 5(a). In contrast, while the external field cannot drive one-photon transitions between hydrogenic energy levels in regime (II), it can efficiently do so between the low-angular-momentum states (with nonvanishing quantum defects) of the alkali atom. Hence, the functional n_0 dependence of the alkali threshold remains unaffected when proceeding from regime (I) to regime (II) for lithium atoms, as observed in the plot.

In regime (III), however, also the alkali-metal spectrum does no more offer any near-resonant one-photon transitions to the external field. Starting from $n_0=41$ (and progressively so for lower principal quantum numbers), the transition $|n_0,\ell_0=0\rangle\rightarrow|n_0,\ell_0=1\rangle$ demands more energy than offered by one single photon of the drive. In this regime our numerical ionization threshold tends to the same algebraic dependence on n_0 as observed in the low-frequency experiment on lithium, which was attributed to a series of Landau-Zener transitions connecting the atomic initial state to the atomic continuum in Ref. [22]. Since the lithium experiment [22] was performed with rather low principal quantum numbers, at a low frequency of the drive, the transition from regime (III) to regime (II) could not be observed in this experiment. Our above analysis of the numerical results leads to the prediction that this transition will occur only at $n_0\simeq 54$, where the driving frequency $\omega/2\pi=15$ GHz matches the transition $|n_0=54,\ell_0=0\rangle\rightarrow|n_0=54,\ell_0=1\rangle$. Since these experiments additionally employed longer atom-field interaction times, the transition will furthermore be observed at lower field amplitudes as compared to our numerical experiment. This, however, leaves the functional dependence of $F_{10\%}$ on n_0 unaffected, consistent with our discussion of Fig. 4.

Let us finally interpret our results in the context of classical-quantum correspondence discussed in the Introduction above. For this purpose, we have plotted the laboratory hydrogen data and the numerical lithium data of Fig. 5(a) in classically scaled variables $F_0 = F n_0^4$ and $\omega_0 = \omega n_0^3$ (which are inherited from the scale invariance of the classical equations of motion describing the driven two-body Coulomb problem [74]) in Fig. 5(b). Here this is perfectly legitimate, since both these datasets were obtained for precisely the same values of n_0, ω, and t—and the use of scaled variables does therefore not imply any additional hypothesis. Hence, in this plot, all hydrogen data can be identified with a well-defined classical phase-space structure, fixed through F_0 and ω_0 [21,74]. We see that the smaller slope of the threshold in the large-n_0 part of Fig. 5(a) translates into increasing thresholds in Fig. 5(b), for increasing scaled frequencies, above $\omega_0 \simeq 0.4$ (for Li) and $\omega_0 \simeq 0.85$ (for H). This is a clear signature of dynamical localization [10,12,75], which stabilizes the atom against chaotic ionization through quantum interference effects [13–15,76], and is here unambiguously reproduced also by the lithium data—in the absence of a well-defined classical analog. Obviously, however, a sequence of near-resonant one-photon transitions—with quasirandom detunings from exact resonance, leading to strong fluctuations in the corresponding transition matrix elements [16,63]—connecting the atomic initial state to the continuum is easily established for the lithium atom, even down to lower values of n_0, due to the core-induced energy shift of the low-angular-momentum states. Consequently, efficient ionization of lithium remains possible in regime (II), where the hydrogenic thresholds increase with decreasing ω_0, leading to an increasing gap between the alkali-metal and the hydrogen thresholds for $\omega_0 < 0.8$. It is precisely in these parameter regimes (II) and (III) that all experimental data on nonhydrogenic Rydberg states have been obtained so far [2,12,23], thus explaining the apparently enhanced ionization of nonhydrogenic alkali-metal Rydberg states [28]. Alkali Rydberg states therefore provide a perfect scene for quantum chaos, which, much as quantum mechanics compared to classical mechanics, has to host a larger class of systems than classical chaos: sequences of near-resonant one-photon transitions (with quasirandom detunings) can be induced by classical chaos (as they are in periodically driven atomic hydrogen), but equally so by quantum phase shifts due to core scattering, unavailable in the classical dynamics of a point particle.

V. SUMMARY

We have given a detailed description of the *ab initio* treatment of microwave driven alkali-metal Rydberg states in the parameter regime of state of the art laboratory experiments. Unaffected by pragmatic considerations (such as the availability of laser sources to excite the initial Rydberg level from the atomic ground state [20]) which mostly lead the experimentalists to perform experiments on different atomic species in slightly different parameter regimes, we are now able to compare the ionization dynamics of Li Rydberg states to the one of atomic hydrogen, in precisely the same parameter regime, with the nonvanishing quantum defect of the alkali-metal initial state as the only essential difference. Our numerical experiment followed the laboratory experiment step by step:

(i) measurement of the ionization yield vs driving field amplitude, at fixed driving field frequency and interaction time, for a given quantum number n_0 of the initial state;

(ii) deduction of the ionization threshold from (i), for different values of n_0; and

(iii) comparison to the classical, driven two-body Coulomb dynamics, in scaled variables F_0 and ω_0;

and allowed us to identify the cause of the apparently enhanced ionization of nonhydrogenic alkali-metal Rydberg states. Furthermore, it led us to the unexpected prediction that nonhydrogenic and alkali-metal Rydberg states should exhibit quantitatively comparable thresholds in the frequency regime $\omega_0 > 1$—so far unexplored in the laboratory.

ACKNOWLEDGMENTS

The CPU time was provided by the RZG of the Max-Planck-Gesellschaft, on a CRAY T3E, and by the LRZ of the Bayerische Akademie der Wissenschaften, on a HITACHI SR8000-F1. We acknowledge ever entertaining and fruitful discussions with D. Delande on the implementation of the *R*-matrix method in Ref. [41], and partial financial support by the DAAD (through PROCOPE).

---

[1] J.E. Bayfield and P.M. Koch, Phys. Rev. Lett. **33**, 258 (1974).
[2] M.W. Noel, M.W. Griffith, and T.F. Gallagher, Phys. Rev. A **62**, 063401 (2000).
[3] D. Kleppner, M. G. Littman, and M. L. Zimmermann, Sci. Am. May, 108 (1981).
[4] J.G. Leopold and I.C. Percival, Phys. Rev. Lett. **41**, 944 (1978).
[5] N.B. Delone, B.A. Zon, and V.P. Krainov, Zh. Eksp. Teor. Fiz. **75**, 445 (1978).
[6] B.I. Meerson, E.A. Oks, and P.V. Sasorov, Pis'ma Zh. Eksp. Teor. Fiz. **29**, 79 (1979).
[7] J.G. Leopold and D. Richards, J. Phys. B **19**, 1125 (1986).
[8] B.V. Chirikov, in *Chaos and Quantum Physics*, Proceedings of the Les Houches, Summer School, Session LII, edited by M.-J. Giannoni, A. Voros, and J. Zinn-Justin (North-Holland, Amsterdam, 1989).
[9] A. Einstein, Verh. Dtsch. Phys. Ges. **9/10**, 82 (1917).
[10] E.J. Galvez, B.E. Sauer, L. Moormann, P.M. Koch, and D. Richards, Phys. Rev. Lett. **61**, 2011 (1988).
[11] T.F. Gallagher, C.F. Mahon, P. Pillet, P. Fu, and J.B. Newman, Phys. Rev. A **39**, 4545 (1989).
[12] M. Arndt, A. Buchleitner, R.N. Mantegna, and H. Walther, Phys. Rev. Lett. **67**, 2435 (1991).
[13] S. Fishman, D.R. Grempel, and R. Prange, Phys. Rev. Lett. **49**, 509 (1982).
[14] R. Blümel and U. Smilansky, Phys. Rev. Lett. **52**, 137 (1984).
[15] G. Casati, B.V. Chirikov, and D.L. Shepelyansky, Phys. Rev. Lett. **53**, 2525 (1984).

[16] N. Brenner and S. Fishman, J. Phys. A **29**, 7199 (1996).
[17] M. Courtney, N. Spellmeyer, H. Jiao, and D. Kleppner, Phys. Rev. A **51**, 3604 (1995).
[18] G. Benenti, G. Casati, and D.L. Shepelyansky, Phys. Rev. A **57**, 1987 (1998).
[19] D. Campos, M.C. Spinel, and J. Madroñero, J. Phys. A **34**, 8101 (2001).
[20] O. Benson, A. Buchleitner, M. Arndt, R.N. Mantegna, and H. Walther, Phys. Rev. A **51**, 4862 (1995).
[21] P.M. Koch and K.A.H. Leeuwen, Phys. Rep. **255**, 289 (1995).
[22] C.R. Mahon, J.L. Dexter, P. Pillet, and T.F. Gallagher, Phys. Rev. A **44**, 1859 (1991).
[23] A. Buchleitner, D. Delande, J. Zakrzewski, R.N. Mantegna, M. Arndt, and H. Walther, Phys. Rev. Lett. **75**, 3818 (1995).
[24] Panming Fu, T.J. Scholz, J.M. Hettema, and T.F. Gallagher, Phys. Rev. Lett. **64**, 511 (1990).
[25] H.B. van Linden van den Heuvell and T.F. Gallagher, Phys. Rev. A **32**, 1495 (1985).
[26] A. Krug and A. Buchleitner, Europhys. Lett. **49**, 176 (2000).
[27] A. Krug and A. Buchleitner, Phys. Rev. Lett. **86**, 3538 (2001).
[28] A. Krug, Ph.D. thesis, Ludwig-Maximilians-Universität, München, 2001, available at www.ub.uni-muenchen.de/elektronische-dissertationen/physik/Krug Andreas.pdf.
[29] A. Krug and A. Buchleitner, Comput. Phys. Commun. **147**, 394 (2002).
[30] M.G. Floquet, Ann. Ec. Normale Supér. **12**, 47 (1883).
[31] Y.B. Zeldovich, Sov. Phys. JETP **24**, 1006 (1967).
[32] J.H. Shirley, Phys. Rev. **138**, B979 (1965).
[33] C. Kittel and C.Y. Fong, *Quantentheorie der Festkörper*, 3rd ed. (Oldenbourg, München, 1989) .
[34] M. Reed and B. Simon, *Modern Methods in Mathematical Physics* (Academic Press, New York, 1979), Vol. III.
[35] E. Balslev and J.M. Combes, Commun. Math. Phys. **22**, 280 (1971).
[36] K. Yajima, Commun. Math. Phys. **87**, 331 (1982).
[37] Y.K. Ho, Phys. Rep. **99**, 2 (1983).
[38] S. Graffi, V. Grecchi, and H.J. Silverstone, Ann. Inst. Henri Poincaré **42**, 215 (1985).
[39] A. Buchleitner, B. Grémaud, and D. Delande, J. Phys. B **27**, 2663 (1994).
[40] N. Moiseyev, Phys. Rep. **302**, 211 (1998).
[41] M.H. Halley, D. Delande, and K.T. Taylor, J. Phys. B **26**, 1775 (1993).
[42] U. Fano, Phys. Rev. A **24**, 619 (1981); D.A. Harmin, *ibid.* **24**, 2491 (1981).
[43] M.J. Seaton, Rep. Prog. Phys. **46**, 167 (1983); the extension to Coulomb functions with complex position and energies is outlined in Ref. [41].
[44] M. Reed and B. Simon, *Modern Methods in Mathematical Physics* (Academic Press, New York, 1980), Vol.I.
[45] C.W. Clark and K.T. Taylor, J. Phys. B **15**, 1175 (1982).
[46] D. Delande and J.C. Gay, J. Phys. B **19**, L173 (1986).
[47] G.B. Arfken and H.J. Weber, *Mathematical Methods for Physicists* (Academic Press, San Diego, 1995).
[48] A. Buchleitner, D. Delande, and J.-C. Gay, J. Opt. Soc. Am. B **12**, 505 (1995).
[49] R. Blümel and U. Smilansky, Z. Phys. D: At., Mol. Clusters **6**, 83 (1987).
[50] H.P. Breuer and M. Holthaus, Z. Phys. D: At., Mol. Clusters **11**, 1 (1989).
[51] A. Buchleitner and D. Delande, Chaos, Solitons Fractals **5**, 1125 (1995).
[52] A. Buchleitner, Ph.D. thesis, Université Pierre et Marie Curie, Paris, 1993.
[53] C.J. Lorenzen and K. Niemax, Phys. Scr. **27**, 300 (1983).
[54] R. Shakeshaft, Z. Phys. D: At., Mol. Clusters **8**, 47 (1988).
[55] E. Cormier and P. Lambropoulos, J. Phys. B **29**, 1667 (1996).
[56] T. Ericsson and A. Ruhe, Math. Comput. **35**, 1251 (1980).
[57] D. Delande, A. Bommier, and J.C. Gay, Phys. Rev. Lett. **66**, 141 (1991).
[58] A. Buchleitner, K. Taylor, and D. Delande (unpublished).
[59] A. Buchleitner and D. Delande, Phys. Rev. A **55**, R1585 (1997).
[60] G.N. Rockwell, V.F. Hoffman, Th. Clausen, and R. Blümel, Phys. Rev. A **65**, 025401 (2002).
[61] M. Pont and R. Shakeshaft, Phys. Rev. A **44**, 4110 (1991).
[62] A. Buchleitner, I. Guarneri, and J. Zakrzewski, Europhys. Lett. **44**, 162 (1998).
[63] S. Wimberger and A. Buchleitner, J. Phys. A **63**, 7181 (2001).
[64] R.B. Shirts and W.P. Reinhardt, J. Chem. Phys. **77**, 5204 (1982); **79**, 3173 (1983).
[65] R.S. MacKay, J.D. Meiss, and I.C. Percival, Phys. Rev. Lett. **52**, 697 (1984).
[66] J.D. Meiss and E. Ott, Phys. Rev. Lett. **55**, 2741 (1985).
[67] T. Geisel, G. Radons, and J. Rubner, Phys. Rev. Lett. **57**, 2883 (1986).
[68] Y.-C. Lai, C. Grebogi, R. Blümel, and M. Ding, Phys. Rev. A **45**, 8284 (1992).
[69] G. Benenti, G. Casati, G. Maspero, and D.L. Shepelyansky, Phys. Rev. Lett. **84**, 4088 (2000).
[70] R. Ketzmerick, L. Hufnagel, F. Steinbach, and M. Weiss, Phys. Rev. Lett. **85**, 1214 (2000).
[71] O.E. Alon and N. Moiseyev, Phys. Rev. A **46**, 3807 (1992).
[72] J. Main and G. Wunner, J. Phys. B **27**, 2835 (1994).
[73] A. Buchleitner and D. Delande, Phys. Rev. Lett. **70**, 33 (1993).
[74] I.C. Percival, Proc. R. Soc. London, Ser. A **353**, 289 (1977).
[75] J.E. Bayfield, G. Casati, I. Guarneri, and D.W. Sokol, Phys. Rev. Lett. **63**, 364 (1989).
[76] G. Casati, B.V. Chirikov, D.L. Shepelyansky, and I. Guarneri, Phys. Rep. **154**, 77 (1987).